still shows decent resist quality after 10 months of storage in air (fig. S21). This proposed mechanism is further corroborated by the fact that (i) B-doped nanowires grown without pressure modulation only yielded uniform etching structures (fig. S22) (*18*,*19*); (ii) intentional gold diffusion only at the end of *p*-type nanowire synthesis also yielded etch resist (fig. S23); (iii) diffused Au did not recruit B (figs. S14 and S15), which is known to affect Si etching; and (iv) possible B incorporation directly from the gas phase is along the spicule radial direction, which is orthogonal to the direction for resist formation. Overall, we showed that dopant incorporation or nanowire initial morphology itself cannot yield the observed complex structures. The curvatures of the final spicules are defined by the shapes of patterned resists, curved catalyst/Si interfaces, crystallographic orientations, and etching conditions (fig. S24). The initial isolated Au nanoparticles play multiple roles, such as catalyzing Si growth, defining edge curvature, and supplying diffused Au atoms and clusters (fig. S25). Finally, we note that because metal diffusion along semiconductor surfaces is general, as in GaP-Au (*15*), GaAs-Au (*15*), and Si-In/Sn (*10*) systems, a similar patterning and lithography approach may be applied in other semiconductors.

The anisotropic mesoscale texture of Si spicules suggests that they may have different interactions with surrounding matrices such as hydrogels or biological tissues, as compared to other more isotropic Si structures such as diameter-modulated nanowires (*18*, *19*). To test this possibility, we first mounted single mesostructured Si spicules (<112>-oriented, *p*-type) onto atomic force microscopy (AFM) cantilever tips with a focused ion-beam system (Fig. 4A, inset). Next, by approaching/retracting the spicules to/from collagen type I hydrogel [materials and methods in (*18*) and fig. S26], we were able to monitor the force and work of the spicule-matrix interactions in both the forward and reverse directions. For each recording, we chose a fresh location over the hydrogel surface. To study the effects of probe geometry and surface, we performed control measurements (figs. S26 and S27) with an un-etched Si nanowire, a uniform diameter-modulated Si nanowire (*18*, *19*), and a nanoporous Si nanowire (*18*). A representative force-distance (*F-D*) curve recorded from the Si spicule probe exhibits a detachment force of ~3.9 nN and a detachment work of ~15.6 fJ (Fig. 4A). Statistical analyses of *F-D* measurements with the single Si spicule and different Si nanowire probes (Fig. 4, B and C; $n = 50$ *F-D* curves per probe) demonstrates that the anisotropic mesostructure, rather than surface area or nanoscale roughness, yields a major enhancement in detachment force and detachment work (figs. S26 and S27). The observation that the anisotropic spicule requires the largest detachment force from collagen is reminiscent of natural systems, such as a bee's stinger, which can become rooted in skin. This suggests the potential of adopting mesostructured Si spicules for building tight junctions with other soft materials, such as in tissue-interfacing adhesives or bioelectronics.

REFERENCES AND NOTES

1. S. Tawfick *et al.*, *Adv. Mater.* **24**, 1628–1674 (2012).
2. S. Xu *et al.*, *Science* **347**, 154–159 (2015).
3. J. A. Rogers, T. Someya, Y. Huang, *Science* **327**, 1603–1607 (2010).
4. V. B. Shenoy, D. H. Gracias, *MRS Bull.* **37**, 847–854 (2012).
5. S. Mann, G. A. Ozin, *Nature* **382**, 313–318 (1996).
6. G. V. Naik, V. M. Shalaev, A. Boltasseva, *Adv. Mater.* **25**, 3264–3294 (2013).
7. T. Ozel, G. R. Bourret, C. A. Mirkin, *Nat. Nanotechnol.* **10**, 319–324 (2015).
8. M. Cusack, A. Freer, *Chem. Rev.* **108**, 4433–4454 (2008).
9. O. Moutanabbir *et al.*, *Nature* **496**, 78–82 (2013).
10. W. H. Chen *et al.*, *Nat. Commun.* **5**, 4134 (2014).
11. E. R. Hemesath *et al.*, *Nano Lett.* **12**, 167–171 (2012).
12. N. Ferralis, F. El Gabaly, A. K. Schmid, R. Maboudian, C. Carraro, *Phys. Rev. Lett.* **103**, 256102 (2009).
13. P. Madras, E. Dailey, J. Drucker, *Nano Lett.* **10**, 1759–1763 (2010).
14. J. B. Hannon, S. Kodambaka, F. M. Ross, R. M. Tromp, *Nature* **440**, 69–71 (2006).
15. K. A. Dick, K. Deppert, L. Samuelson, L. R. Wallenberg, F. M. Ross, *Nano Lett.* **8**, 4087–4091 (2008).
16. M. I. den Hertog *et al.*, *Nano Lett.* **8**, 1544–1550 (2008).
17. J. E. Allen *et al.*, *Nat. Nanotechnol.* **3**, 168–173 (2008).
18. See the supplementary materials on *Science* Online.
19. J. D. Christesen, C. W. Pinion, E. M. Grumstrup, J. M. Papanikolas, J. F. Cahoon, *Nano Lett.* **13**, 6281–6286 (2013).
20. S. K. Lim, S. Crawford, G. Haberfehlner, S. Gradečak, *Nano Lett.* **13**, 331–336 (2013).
21. I. R. Musin, D. S. Boyuk, M. A. Filler, *J. Vac. Sci. Technol. B* **31**, 020603 (2013).
22. F. M. Ross, J. Tersoff, M. C. Reuter, *Phys. Rev. Lett.* **95**, 146104 (2005).
23. R. E. Algra *et al.*, *Nature* **456**, 369–372 (2008).
24. R. W. Day *et al.*, *Nat. Nanotechnol.* **10**, 345–352 (2015).
25. L. Zhao, A. C. L. Siu, J. A. Petrus, Z. He, K. T. Leung, *J. Am. Chem. Soc.* **129**, 5730–5734 (2007).
26. O. C. Hellman, J. A. Vandenbroucke, J. Rüsing, D. Isheim, D. N. Seidman, *Microsc. Microanal.* **6**, 437–444 (2000).
27. N. A. Stolwijk, B. Schuster, J. Holzl, H. Mehrer, W. Frank, *Physica B+C* **116**, 335–342 (1983).
28. H. Seidel, L. Csepregi, A. Heuberger, H. Baumgartel, *J. Electrochem. Soc.* **137**, 3612–3626 (1990).
29. L. C. Chen, M. J. Chen, C. H. Lien, C. C. Wan, *J. Electrochem. Soc.* **142**, 170–176 (1995).
30. B. Mehta, M. Tao, *J. Electrochem. Soc.* **152**, G309–G315 (2005).

ACKNOWLEDGMENTS

This work is supported by NSF [NSF CAREER, grant DMR-1254637; and NSF Materials Research Science and Engineering Centers (MRSEC), grant DMR-0820054], the Searle Scholars Foundation, the Air Force Office of Scientific Research (grant AFOSR FA9550-14-1-0175), and the University of Chicago startup fund. APT was performed at NUCAPT, whose APT was purchased and upgraded with funding from NSF–Major Research Instrumentation Program (grant DMR-0420532) and the Office of Naval Research–Defense University Research Instrumentation Program (grants N00014-0400798, N00014-0610539, and N00014-0910781). Instrumentation at NUCAPT was further upgraded by the Initiative for Sustainability and Energy at Northwestern. This work also made use of the EPIC facility (NUANCE Center–Northwestern University), which has received support from the NSF MRSEC program (grant NSF DMR-1121262) at the Materials Research Center and from the International Institute for Nanotechnology (IIN); and the State of Illinois, through the IIN. Part of this research is sponsored by the Air Force Research Laboratory (grant FA9550-12-1-0280). The authors thank L. Yu, Q. Guo, J. Jureller, J. Austin II, Y. Chen, S.-I. Baik, and T. A. Witten for technical support and stimulating discussion.

SUPPLEMENTARY MATERIALS

www.sciencemag.org/content/348/6242/1451/suppl/DC1
Materials and Methods
Supplementary Text
Figs. S1 to S27
References (*31*–*35*)

11 June 2014; accepted 19 May 2015
10.1126/science.1257278

HIGH-PRESSURE PHYSICS

Direct observation of an abrupt insulator-to-metal transition in dense liquid deuterium

M. D. Knudson,[1]* M. P. Desjarlais,[1] A. Becker,[2] R. W. Lemke,[1] K. R. Cochrane,[1] M. E. Savage,[1] D. E. Bliss,[1] T. R. Mattsson,[1] R. Redmer[2]

Eighty years ago, it was proposed that solid hydrogen would become metallic at sufficiently high density. Despite numerous investigations, this transition has not yet been experimentally observed. More recently, there has been much interest in the analog of this predicted metallic transition in the dense liquid, due to its relevance to planetary science. Here, we show direct observation of an abrupt insulator-to-metal transition in dense liquid deuterium. Experimental determination of the location of this transition provides a much-needed benchmark for theory and may constrain the region of hydrogen-helium immiscibility and the boundary-layer pressure in standard models of the internal structure of gas-giant planets.

In 1935, Wigner and Huntington (*1*) were the first to predict that when squeezed to sufficiently high density (ρ) and pressure (*P*), hydrogen would undergo a density-driven transition from an insulating, molecular solid to a conducting, atomic solid. Subsequently, this fundamental question of precisely how and at what *P* hydrogen metallizes at low temperature (*T*) has become one of the longest-standing open questions of high-pressure physics (*2*). More recently, there has been much interest in the analogous molecular insulator to atomic metal transition in the liquid at low *T* just above the melt line, largely due to its relevance to planetary science (*3*, *4*). A metallization transition in this region could provide a constraint for the

[1]Sandia National Laboratories, Albuquerque, NM, USA. [2]Institute of Physics, University of Rostock, Rostock, Germany.
*Corresponding author. E-mail: mdknuds@sandia.gov

low-*P* boundary of the region of hydrogen-helium immiscibility; first-principles calculations suggest that hydrogen metallization acts as a catalyst for hydrogen-helium demixing (*5*). This phenomenon, resulting in an additional energy source through latent heat and gravitational settling of helium, may play an important role in the evolution of the gas giants and has been proposed as a possible solution to the luminosity problem of Saturn (*3*, *4*). This phenomenon could also provide justification for the presence of a layer boundary in the interior of gas-giant planets, a necessary feature of the often-used three-layer model (*6*), which has shown reasonable success in describing observables of Jupiter and Saturn (*7*).

Experimental observation of this transition would also provide a benchmark for first-principles theoretical models of this phenomenon that fall into the category of density functional theory (DFT) within the generalized gradient approximation (GGA). Studies (*8*–*10*) using semilocal density functionals (DF), such as Perdew-Burke-Ernzerhof (PBE) (*11*), suggest the presence of a first-order liquid-liquid, insulator-to-metal transition (LL-IMT). The transition boundary in pressure-temperature (*PT*) space ends in a critical point at ~1500 to 2000 K, with negative slope (*dT*/*dP*) between ~2000 and 800 K and ~100 and 200 GPa (Fig. 1). This transition is predicted to be a ρ-driven dissociative transition in the liquid and appears similar to the so-called plasma phase transition (PPT) suggested to exist as a first-order transition in the partially ionized plasma domain at finite *T* (*12*, *13*). However, the DFT simulations predict this transition in the dense liquid at considerably lower *T* and higher *P*, analogous to the long-ago proposed IMT in the solid (*1*, *2*).

More recent studies (*14*, *15*) have looked at nonlocal functionals such as the hybrid Heyd-Scuseria-Ernzerhof (HSE) (*16*) and the van der Waals vdW-DF2 (*17*), as well as nuclear quantum effects (NQE) through the use of path integral molecular dynamics (PIMD) methods. We investigated vdW-DF2 and a second van der Waals functional, vdW-DF1 (*18*, *19*). These nonlocal DFs predict a transition *P* between ~200 and 400 GPa (Fig. 1) and also exhibit a critical point at ~2000 K (*18*). A phase boundary as high as ~400 to 600 GPa has been predicted using quantum Monte Carlo (QMC) techniques (*20*). Although all of these first-principles approaches exhibit a first-order LL-IMT in the warm dense fluid, the transition *P* and ρ are extremely sensitive to the choice of method and DF. This results in a predicted transition *P* that differs by as much as 400 to 500 GPa and a ρ at the transition of ~0.75 to 1.5 g/cc for hydrogen and ~1.5 to 3 g/cc for deuterium (figs. S19 and S20).

Earlier shock-wave reverberation experiments observed a continuous IMT via electrical conductivity measurements at ~140 GPa (measured) and ~3 kK (calculated) (*21*–*23*). In a similar *P* (calculated) and *T* (calculated) range, another group reported observation of an increase in ρ in conjunction with the continuous increase in conductivity (*24*). The IMT has also been explored in the predominately *T*-driven regime (~40 to 100 GPa and ~5 to 20 kK) through precompressed laser-shock experiments (*25*, *26*). However, these results are at considerably higher *T*, above the predicted critical points reported in the first-principles studies (figs. S19 and S20). High-*P* studies of the solid hydrogen phase diagram have not reported metallization (*2*, *27*). Static measurements have interpreted plateaus in the *T*-laser power curve as an observation of latent heat of a LL transition (*28*). However, the source of these plateaus could be due to changes in thermal conduction or the optical properties of the sample instead of a first-order transition (*29*).

Here, we present the results of a series of dynamic compression experiments on liquid deuterium performed at the Sandia Z machine (*30*), a pulsed-power generator capable of producing large pulsed currents (~20 MA) and magnetic field densities (~10 MG) within a low inductance load. These current and field densities produce magnetic pressures of several hundred GPa. The pulsed nature of the experiment allows inertia to hold the load assembly together for the duration of interest. With proper design of the experimental configuration and precise current pulse shaping, liquid deuterium samples were driven to more than 300 GPa while remaining below 1800 K. These experiments show a dramatic increase in reflectivity of the deuterium samples, indicative of an abrupt increase in conductivity between 280 and 305 GPa. We interpret this signal as evidence of an abrupt, ρ-driven LL-IMT.

Liquid deuterium samples were condensed in a cryocell (Fig. 2 and fig. S3) by filling a cavity with high-purity deuterium gas at 124 kPa (18 pounds per square inch) and cooling the cryocell to 22.0 ± 0.1 K, producing a quiescent liquid sample with nominal initial ρ of 0.167 g/cc (±0.4%). The cryocell was positioned a short distance from an aluminum electrode. Upon discharge of the accelerator capacitor banks, a shaped current pulse flowed through the experimental load. The initial increase in current accelerated the electrode across the gap, producing a shock within the front plate of the cryocell at impact, resulting in a series of shock-wave reverberations that stepwise-loaded the deuterium sample to ~800 to 1400 K, depending on the experiment. The subsequent increase in current drove a ramp compression wave into the cryocell, further compressing the deuterium sample along an isentrope to peak *P* and ρ of more than 300 GPa and 2 g/cc. Varying the magnitude of the initial shock enabled access to different *T* isentropes, allowing a range of *PT* space to be explored.

The liquid deuterium samples were diagnosed using fiber-optic–coupled diagnostics. A velocity interferometer (VISAR) (*31*) measured the velocity of the aluminum/deuterium and the deuterium/LiF interface (reflecting off an aluminum coating on the LiF window), using 532-nm laser light. Spectrally and temporally resolved reflectivity was measured using a spectrometer (450- to 650-nm bandwidth) coupled to a streak camera. The interferometer signal from the deuterium sample (Fig. 2) originally reflecting off the aluminum/deuterium interface is lost at ~2650 ns (~120 GPa). The signal suddenly reappears at ~2800 ns (~280 GPa), only to abruptly disappear again upon decompression at ~2880 ns (as *P* drops below ~280 GPa). In contrast, the interferometer signal reflecting from the deuterium/LiF interface is maintained throughout the experiment, albeit with a transient drop at ~2780 to 2800 ns that slightly precedes the reemergence of the signal originating from the aluminum/deuterium interface.

The spectral dependence of the reflected signal was obtained by determining the relative reflectivity with respect to aluminum (*18*) as a function of wavelength and time (Fig. 3). Before the loss of

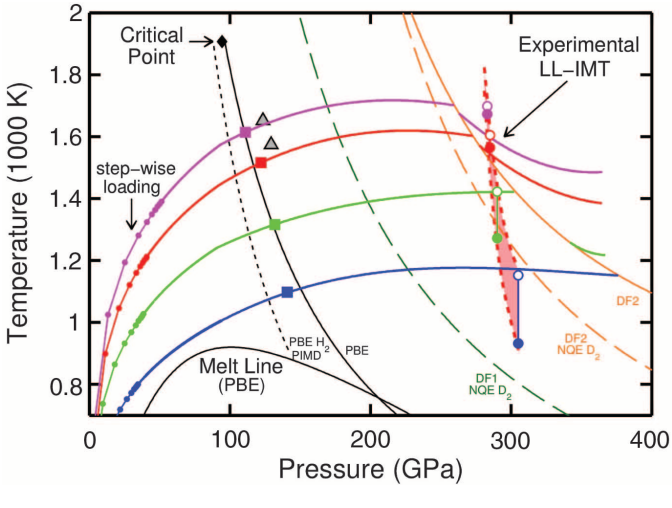

Fig. 1. Deuterium *PT* diagram. Melt line, (*9*). Theoretical LL-IMT phase boundaries: Black line, PBE (*9*); short dashed black line, PBE+PIMD (*15*); dashed green line, vdW-DF1+NQE for deuterium (this work); orange line, vdW-DF2 (this work); dashed orange line, vdW-DF2 +NQE for deuterium (this work). Experiment: gray triangles (*28*). The experimental *PT* paths from this work are shown as the nearly horizontal solid lines, the result of stepwise loading (shock reverberation) followed by ramp compression. The colored squares at ~120 to 150 GPa indicate where the deuterium is observed to become opaque as the band gap closes to ~2.1 eV. The shaded red region indicates the experimentally determined location of the LL-IMT. Open circles denote the estimated *T* at the phase boundary, neglecting any latent heat, and the closed circles include an estimate of the latent heat obtained by matching isentropes on either side of the phase boundary through thermodynamic integration using the vdW-DF2 functional (*18*). See (*18*) for an expanded version of this figure.

signal at ~120 GPa, the reflectivity ratio is essentially unity, indicating that the reflection is occurring at the aluminum/deuterium interface (i.e., the deuterium is transparent). Upon reappearance of the signal at ~280 GPa, a reflectivity ratio of just over 60% is observed throughout the visible range of 450 to 650 nm (1.9 to 2.75 eV) (Fig. 3C). DFT simulations of aluminum at these conditions (~1000 K and ~300 GPa) suggest an aluminum reflectivity in this wavelength range of ~72% (fig. S8). This implies an absolute reflectivity measurement in these experiments of ~45% in this wavelength range, consistent with DFT calculations for the atomic fluid phase of hydrogen (fig. S6).

This behavior suggests that, as deuterium is compressed above ~120 GPa, it loses transparency, indicating that the band gap closes to ~2 to 2.5 eV, resulting in strong absorption in the visible spectrum. The inferred band gap from a reanalysis of the Weir *et al.* experiments (*21*–*23*) is consistent with this picture (fig. S17B). Furthermore, DFT simulations of deuterium suggest a sharp increase in the absorption coefficient at a photon energy corresponding to the band gap. The band gap decreases with increasing P and drops below ~2 to 2.5 eV at ~125 to 150 GPa (fig. S9), in reasonable agreement with the experimental observations (fig. S10). Upon further increase in P, the observed sharp increase in deuterium reflectivity is indicative of an abrupt IMT. Consistent with DFT simulations in the metallic fluid, the observed reflectivity (Fig. 3C) is featureless over a broad energy range (1.9 to 2.75 eV). This increase in reflectivity in the visible is concurrent with a dramatic increase in the calculated DC conductivity. The observed absolute reflectivity of ~45% suggests DC conductivity of a few 10^5 S/m (fig. S7), the same magnitude as that observed by Weir *et al.*, albeit at considerably higher T.

The thermodynamic state of the bulk deuterium sample was determined through the measured apparent velocity at the deuterium/LiF interface and numerical simulations. Given the mechanical and optical response of LiF, one can determine P as a function of time, t [$P(t)$], which does not depend upon the deuterium equation of state (EOS), to a precision of ~2 to 3% at the aluminum/deuterium interface (*18*). The resulting $P(t)$ in the deuterium also provides $T(t)$ and $\rho(t)$ for a given deuterium EOS. We performed this using the Kerley03 EOS for deuterium (*32*) (figs. S11 and S12). The resulting PT paths show the majority of the T increase occurring during the first several shock reverberations (Fig. 1 and fig. S12). This happens well within the molecular fluid phase at relatively low P and ρ, where the Kerley03 EOS (*32*) reasonably reproduces Hugoniot measurements of deuterium (*33*, *34*).

DFT simulations suggest that dissociation becomes important at higher P and ρ (*2*). The Kerley03 EOS may not accurately describe the warm dense fluid in this region because it uses the chemical model representation, so we only rely on the EOS to calculate the state of the sample through the shock-wave reverberation portion of the experiment (up to 100 GPa). Further increases in T are modeled using DFT calculations with the vdW-DF2 functional (Fig. 1 and fig. S15). Although the initial trajectory of the DFT isentropes is similar to that of Kerley03, the increase in T with P begins to diminish, eventually becoming negative as the transition P is approached. This behavior is due to the emergence of dissociation, indicating that appreciable dissociation occurs before the first order LL-IMT. Despite exhibiting differences in $T(P)$ along the isentropes, $\rho(P)$ for the various DFT functionals and the Kerley03 EOS are quite similar, varying by only a few percent (*18*), reaching ~2.14 g/cc (~12.8-fold compression) at 320 GPa (fig. S13). Thus, despite not having a direct ρ measurement in these experiments, the measured $P(t)$ provides an accurate estimate of $\rho(t)$.

Several features become apparent when considering the observed optical changes with respect to the thermodynamic state of the deuterium sample (Fig. 4). The small but measurable increase in reflectivity that precedes the abrupt reflectivity increase appears to coincide with the transient drop in the interferometer signal from the aluminum/LiF interface (Fig. 2). This drop in signal is due to a transient loss of contrast in the interferometer system and is explained by the presence of velocity dispersion in the Doppler-shifted light (*18*). The results observed in these experiments are consistent with ~1% peak velocity dispersion (fig. S14), indicating a transient spatial velocity heterogeneity immediately before the substantial increase in reflectivity. This behavior suggests a small (~1 to 2%) ρ discontinuity between the molecular and atomic fluid, indicative of a first-order transition and the emergence of dissociation before the abrupt increase in reflectivity.

The asymmetry in the deuterium reflectivity with P (Fig. 4) is likely explained by the effects of thermal conduction. The observed reflectivity signal emanates from the deuterium/LiF interface, within a few hundred angstrom optical depth (*18*). Hydrodynamic simulations of the experimental configuration indicate a ΔT between the bulk deuterium and LiF of between 800 and 1400 K, depending on the experiment; deuterium is considerably more compressible than LiF, resulting in a much higher T with compression (fig. S15). Because both the molecular fluid and the LiF are poor thermal conductors, the interface T before metallization will be somewhere near the average T of the bulk deuterium and LiF, and a thermal gradient in the deuterium of several hundred K will develop. Upon metallization, the thermal conductivity of the atomic fluid will increase by roughly two orders of magnitude (as determined by vdW-DF2), and the thermal gradient will rapidly

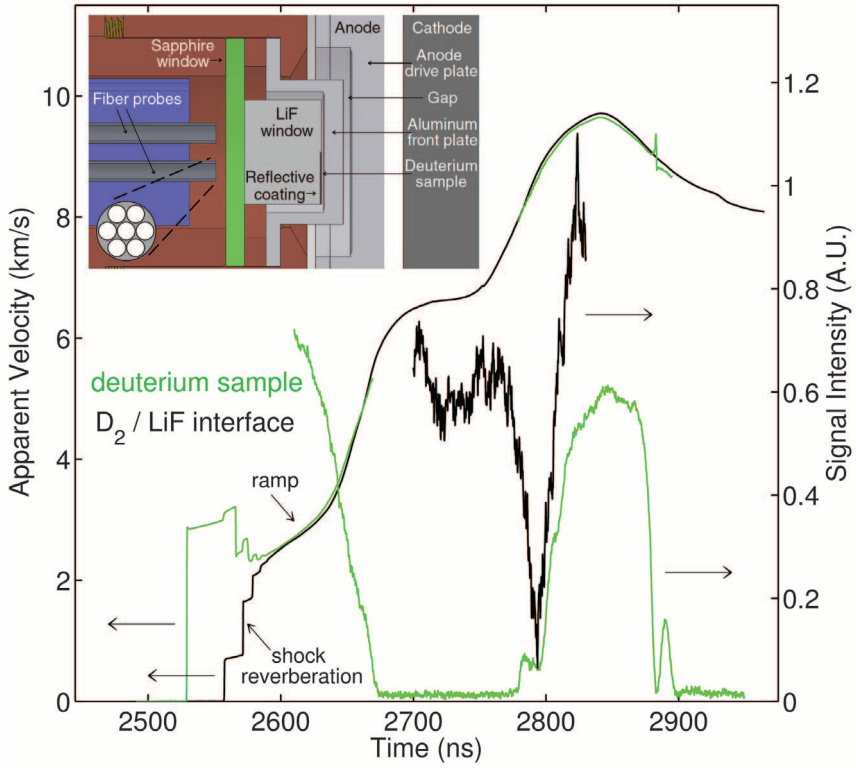

Fig. 2. Experimental profiles. Measured apparent velocities (left axis) from the deuterium sample, originally reflecting from the aluminum/deuterium interface (green line) and the reflective coating on the deuterium/LiF interface (black line). Data correspond to the green PT path in Fig. 1. Also shown are the magnitudes of the interferometer signals from these locations (right axis). The interferometer signal from the deuterium sample is lost as the deuterium becomes opaque due to the band gap closing to ~2.33 eV (the photon energy of the laser), recovers as the deuterium is driven across the IMT, and finally is lost again as the deuterium P drops back below the IMT. The interferometer signal at the deuterium/LiF interface is maintained throughout the duration of the experiment but shows a transient loss of contrast immediately before metallization, indicating the presence of spatial heterogeneity in velocity and, likely, ρ. Inset shows a schematic view of the experimental load (*18*).

diminish as the entire deuterium sample approaches the bulk deuterium T (fig. S16). Therefore, consistent with observation, the change in reflectivity should appear sluggish as P increases and rather sharp as P drops. Due to these effects, the clearest indication of P at the transition boundary corresponds to the abrupt drop in reflectivity upon release in P.

The oscillatory behavior of reflectivity upon further release in P is not fully understood. However, the oscillations are suggestive that the PT path in the experiment is not truly isentropic across the transition. If the transition were indeed first-order, it would not be unexpected in a dynamic experiment for the system to traverse the transition nonisentropically. Furthermore, the effects of thermal conduction at the deuterium/LiF interface may offset any T increase due to latent heat (fig. S16D), resulting in a PT path for deuterium near the interface that is more like an isotherm than an isentrope (*18*). Either of these effects could set up transient features that would oscillate as waves reflect back and forth across the sample cell, which at these conditions is on the order of 10 μm in thickness.

Given that the clearest signature of the transition is upon release in P, there is a complication in estimating T at the transition due to the latent heat. Because we cannot definitively state that the observed transition is first-order, nor can we conclude that a first-order transition would be traversed isentropically in such a dynamic experiment, we consider two extremes. As an upper bound for T at the transition, we consider T along the isentrope at P that coincides with the abrupt drop in reflectivity, neglecting any latent heat. As a lower bound, we use first-principles DFT simulations using the vdW-DF2 functional to estimate the latent heat across the transition through thermodynamic integration (*18*). The resulting bounds are connected by vertical lines in Fig. 1. We note that the effect of thermal conduction at the interface is a further complication in determining T at the transition. The ΔT between the bulk deuterium T and the interface T as P drops back across the transition can be a few hundred K for reasonable values of thermal conductivity of deuterium and LiF (fig. S16). This uncertainty would potentially result in a uniform shift in the boundary shown in Fig. 1 to lower T. Given the relative steepness in dT/dP of the experimentally determined boundary, the uncertainty in T does not result in an appreciable uncertainty in the boundary location in PT space.

With relatively weak dependence on T, as liquid deuterium is compressed to high P the band gap begins to decrease, reaching ~2 to 2.5 eV at ~120 to 150 GPa. The inferred band gap from a reanalysis of the Weir *et al.* experiments (*21*–*23*) is consistent with this picture. This vicinity where we observe extinction of our probe laser and broadband light is very close to where Dzyabura *et al.* (*28*) report the observation of latent heat in their experiments. Attenuation of light as the band gap begins to close, with stronger absorption at higher photon energies, might explain the observed plateau in the T-laser power curve. Upon further compression, signs of dissociation—as evidenced by the onset of reflectivity and the appearance of heterogeneity in velocity and, possibly, ρ—emerge at ~230 to 250 GPa. Finally, a very abrupt increase in reflectivity is observed at ~280 to 305 GPa, indicative of an IMT. The relative insensitivity of the transition to T suggests that this is a ρ-driven transition occurring at ~2 to 2.1 g/cc in deuterium. Although we cannot definitively state that this transition is first-order, the abruptness of the transition, the observed heterogeneity preceding the transition, and the transient oscillations in reflectivity upon release in P back across the transition all suggest that the transition is indeed first-order.

It is instructive to compare and contrast the present study with that performed by Weir *et al.* (*21*, *22*). Both studies used dynamic compression to reach the high-ρ, low-T region of the hydrogen phase diagram. Weir *et al.* were constrained by achievable end states in shock-wave reverberation experiments. By combining lower initial shocks with subsequent ramp compression, we were able to reach both higher ρ and lower T. Both studies

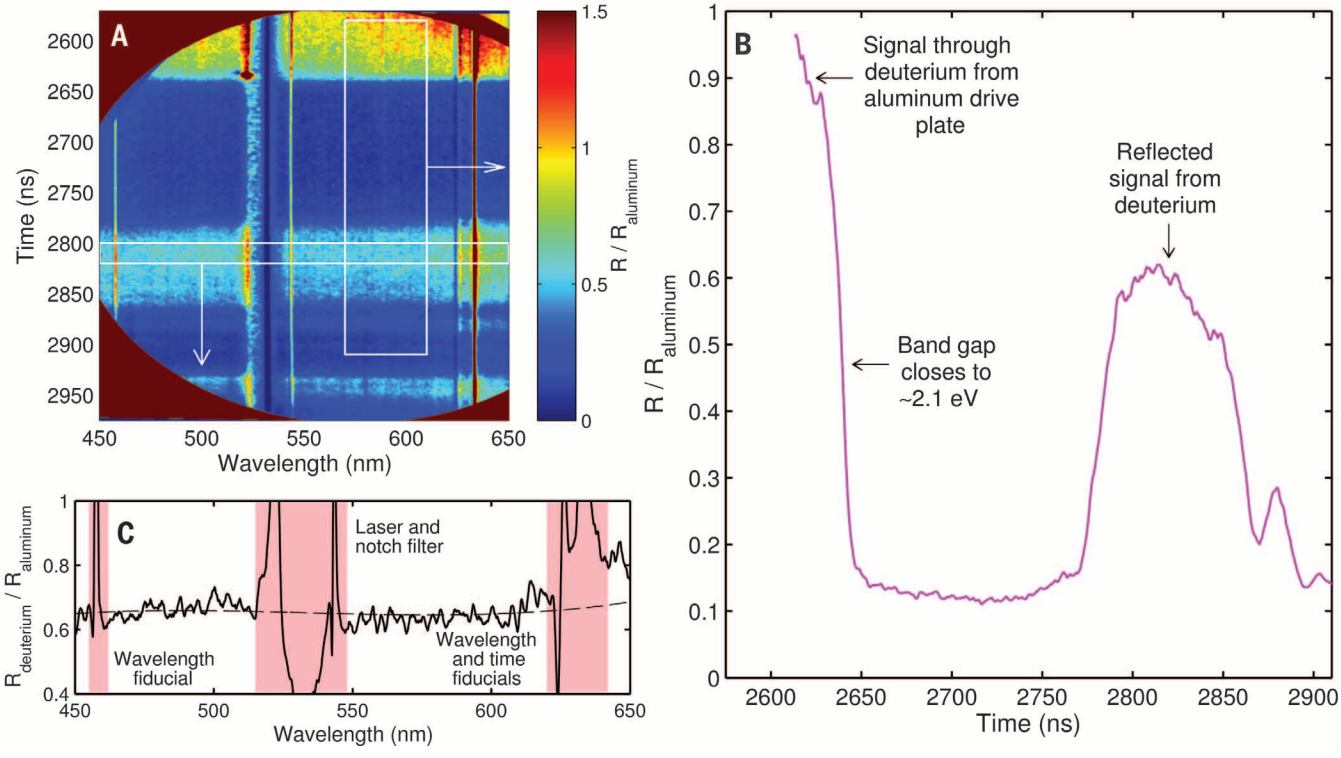

Fig. 3. Spectral and temporal dependence of reflected signal. (**A**) Measured reflectivity with respect to aluminum reflectivity versus both wavelength and time. Data corresponds to the magenta PT path in Fig. 1. (**B**) Line-out of reflectivity with respect to aluminum reflectivity (average over 570 to 610 nm, ~2.1 eV) versus time, showing that, early in time, the reflected signal originates at the aluminum/deuterium interface. Later in time, the deuterium becomes opaque as the band gap closes to ~2 to 2.5 eV and eventually reflective as the deuterium is driven above the IMT. Upon release back below the IMT, the reflectivity is lost. (**C**) Line-out of deuterium reflectivity with respect to aluminum reflectivity (average over 2800 to 2820 ns, during peak compression) versus wavelength, showing a featureless reflectivity ratio of over 60% throughout the visible spectrum. This corresponds to an absolute reflectivity of deuterium of ~45% in the metallic fluid phase (*18*).

measured P and relied on a deuterium EOS and numerical simulation to infer ρ and T. Weir *et al.* measured the DC conductivity at the end state of the shock reverberation and had to perform numerous experiments, each at subsequently higher ρ and T, making it difficult to isolate the relative contribution of ρ and T to the observed gradual increase in conductivity. By directly observing the deuterium sample throughout the experimental duration, we were able to monitor the optical properties of deuterium as a function of ρ at relatively constant T (Fig. 1). Our experiments reveal a very abrupt increase in optical reflectivity correlated with an equally abrupt increase in DC conductivity (as demonstrated in the corresponding DFT calculations), reaching values similar to those reported by Weir *et al.* The relative T insensitivity of this abrupt increase supports our assertion that, at the low T achieved in these experiments, deuterium undergoes a ρ-driven transition to a metallic fluid.

In this regime, the measured LL-IMT boundary P is well above the first-principles GGA predictions, well below the recently proposed QMC boundary, and is in best agreement with the two nonlocal van der Waals functionals. However, the experimentally determined dT/dP is much steeper. At the lowest T (~800 to 1000 K), the observed transition P is more consistent with the vdW-DF1 functional. This is in accordance with the suggestion that the vdW-DF1 functional is more accurate due to better agreement with QMC calculations at 0 K (*35*). However, our results at higher T suggest that this favorable comparison at 0 K may not hold at finite T. At higher T (~1800 K), the observed transition P is somewhat higher than that predicted by the vdW-DF2 functional. This behavior is similar to a detailed comparison of the various DFs with the Weir *et al.* (*21*, *22*) experiments, which probe the IMT at ~3000 K (fig. S18). Finally, Morales *et al.* (*15*) has shown good agreement between measured reflectance from precompressed laser-shock experiments (*25*, *26*) that probe the IMT at even higher T (~5 to 20 kK) to reflectance calculated at the relevant PT conditions using the vdW-DF2 functional. All of these comparisons suggest that the IMT is best described by the nonlocal van der Waals functionals, with perhaps a more complex T dependence, especially at low T (figs. S19 and S20).

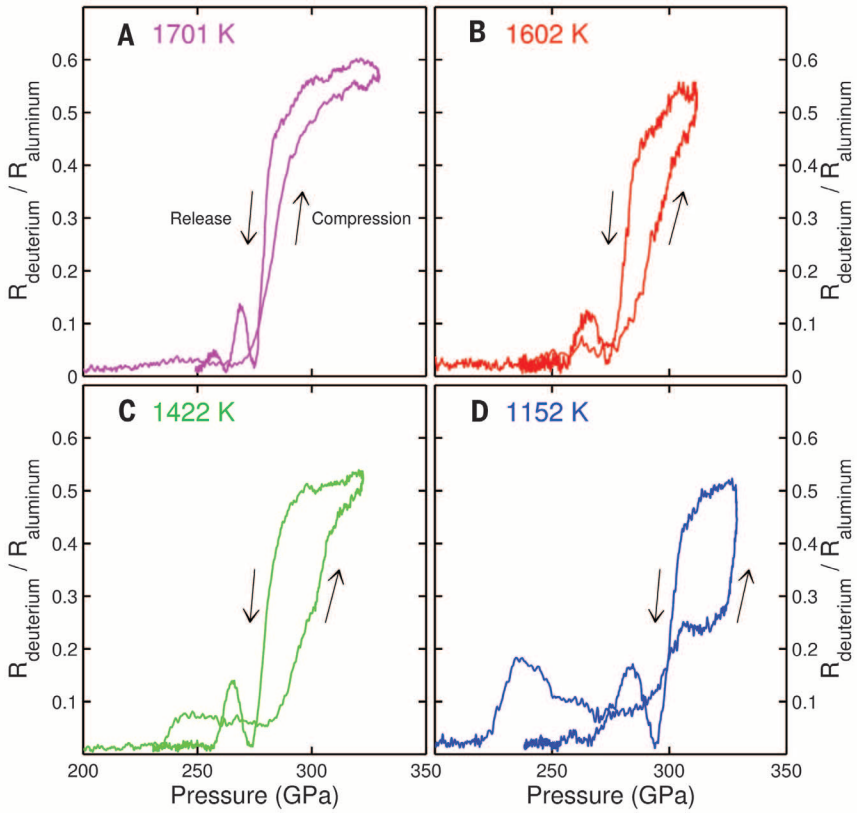

Fig. 4. Reflectivity versus *P*. Measured deuterium reflectivity with respect to aluminum reflectivity (from the interferometer) versus P for each experiment. (**A** to **D**) denote the highest- to lowest-T experiments, respectively. Colors correspond to the PT paths displayed in Fig. 1. T indicated in each panel corresponds to the estimated T at the phase boundary, neglecting any latent heat. All experiments show an asymmetry in the deuterium reflectivity with P; the drop in reflectivity upon P release is considerably sharper than the increase in reflectivity upon compression. This asymmetry, which is more pronounced at lower T, is likely due to the effects of thermal conduction (*18*). All experiments also show a small but measurable reflectivity that precedes the abrupt reflectivity increase, which again is more pronounced at lower T. Finally, all experiments show oscillatory behavior of the reflectivity upon further release of P below the IMT boundary.

In contrast to the gradual, continuous transitions observed in previous higher-T dynamic-compression experiments (*21*, *22*, *25*, *26*), we observe an abrupt LL-IMT at ~300 GPa and ~2 to 2.1 g/cc at low T. These results place a tight constraint on P and ρ of this transition in a regime that is strongly ρ-driven, is predicted to be first-order, and where the largest differences are observed for various first-principles methods and DFs. Furthermore, our results suggest why metallization has been challenging to observe in the solid, because the likely transition P exceeds what is currently achievable with static compression methods with hydrogen. Finally, these results imply that first-principles methods using semilocal DFs such as GGA considerably underestimate P for the LL-IMT in hydrogen at low T. Consequently, estimates for the low-P boundary of the region of hydrogen-helium immiscibility, which have been calculated using GGA (*5*), are likely also considerably underestimated. In addition to providing insight into one of the longest-standing open questions of high-pressure physics, our measurement of the metallization P of hydrogen in the warm dense liquid suggests that the low-P boundary of the immiscibility region should be at or above ~300 GPa. This boundary location will affect the fractions of Saturn and Jupiter that are thought to lie within the immiscibility region and will likely alter our understanding of the structure and evolution of these and other gas-giant planets.

REFERENCES AND NOTES

1. E. Wigner, H. B. Huntington, *J. Chem. Phys.* **3**, 764 (1935).
2. J. M. McMahon, M. A. Morales, C. Pierleoni, D. M. Ceperley, *Rev. Mod. Phys.* **84**, 1607–1653 (2012).
3. R. Smoluchowski, *Nature* **215**, 691–695 (1967).
4. E. E. Salpeter, *Astrophys. J.* **181**, L83 (1973).
5. W. Lorenzen, B. Holst, R. Redmer, *Phys. Rev. B* **84**, 235109 (2011).
6. T. Guillot, *Science* **286**, 72–77 (1999).
7. N. Nettelmann, A. Becker, B. Holst, R. Redmer, *Astrophys. J.* **750**, 52 (2012).
8. I. Tamblyn, S. A. Bonev, *Phys. Rev. Lett.* **104**, 065702 (2010).
9. M. A. Morales, C. Pierleoni, E. Schwegler, D. M. Ceperley, *Proc. Natl. Acad. Sci. U.S.A.* **107**, 12799–12803 (2010).
10. W. Lorenzen, B. Holst, R. Redmer, *Phys. Rev. B* **82**, 195107 (2010).
11. J. P. Perdew, K. Burke, M. Ernzerhof, *Phys. Rev. Lett.* **77**, 3865–3868 (1996).
12. L. D. Landau, Y. B. Zeldovich, *Acta Physico-Chimica U.S.S.R.* **18**, 380 (1943).
13. W. Ebeling, W. Richert, *Phys. Status Solidi B* **128**, 467–474 (1985).
14. W. Lorenzen, A. Becker, R. Redmer, Progress in warm dense matter and planetary physics, in *Frontiers and Challenges in Warm Dense Matter*, F. Graziani, M. P. Desjarlais, R. Redmer, S. B. Trickey, Eds. (Springer, Switzerland, 2014), pp. 203–234.
15. M. A. Morales, J. M. McMahon, C. Pierleoni, D. M. Ceperley, *Phys. Rev. Lett.* **110**, 065702 (2013).
16. J. Heyd, G. Scuseria, M. Ernzerhof, *J. Chem. Phys.* **118**, 8207 (2003).
17. K. Lee, E. D. Murray, L. Kong, B. I. Lundqvist, D. C. Langreth, *Phys. Rev. B* **82**, 081101 (2010).
18. Materials and methods are available as supplementary materials on *Science* Online.
19. M. Dion, H. Rydberg, E. Schröder, D. C. Langreth, B. I. Lundqvist, *Phys. Rev. Lett.* **92**, 246401 (2004).
20. G. Mazzola, S. Yunoki, S. Sorella, *Nat. Commun.* **5**, 3487 (2014).
21. S. T. Weir, A. C. Mitchell, W. J. Nellis, *Phys. Rev. Lett.* **76**, 1860–1863 (1996).
22. W. J. Nellis, S. T. Weir, A. C. Mitchell, *Phys. Rev. B* **59**, 3434–3449 (1999).
23. A reanalysis of the Weir *et al.* experiments (*18*) results in higher inferred T and a systematically larger band-gap energy (~1 eV larger) than those reported in (*21*, *22*).
24. V. E. Fortov *et al.*, *Phys. Rev. Lett.* **99**, 185001 (2007).

25. P. Loubeyre *et al.*, *High Press. Res.* **24**, 25–31 (2004).
26. P. Loubeyre *et al.*, *Phys. Rev. B* **86**, 144115 (2012).
27. A. F. Goncharov *et al.*, *Phys. Rev. B* **87**, 024101 (2013).
28. V. Dzyabura, M. Zaghoo, I. F. Silvera, *Proc. Natl. Acad. Sci. U.S.A.* **110**, 8040–8044 (2013).
29. Z. M. Geballe, R. Jeanloz, *J. Appl. Phys.* **111**, 123518 (2012).
30. M. Matzen *et al.*, *Phys. Plasmas* **12**, 055503 (2005).
31. L. M. Barker, R. E. Hollenbach, *J. Appl. Phys.* **43**, 4669 (1972).
32. G. I. Kerley, Equations of state for composite materials, *Technical Report No. SAND2003-3613*, Sandia National Laboratories (2003).
33. N. C. Holmes, M. Ross, W. J. Nellis, *Phys. Rev. B* **52**, 15835–15845 (1995).
34. J. E. Bailey *et al.*, *Phys. Rev. B* **78**, 144107 (2008).
35. R. C. Clay III *et al.*, *Phys. Rev. B* **89**, 184106 (2014).

ACKNOWLEDGMENTS

We acknowledge the crew of the Sandia Z facility for their contributions to these experiments; L. Shulenburger, J. Benage, and W. Lorenzen for numerous insightful discussions; and support from the Deutsche Forschungsgemeinschaft via SFB 652 and grant Re 882/11-2. A. Becker performed calculations at the North-German Supercomupting Alliance (HLRN). The experiments were performed as part of the Z Fundamental Science Program. Sandia National Laboratories is a multiprogram laboratory managed and operated by Sandia Corporation, a wholly owned subsidiary of Lockheed Martin Corporation, for the U.S. Department of Energy's National Nuclear Security Administration under contract DE-AC04-94AL85000. Data are available in the supplementary materials and upon request to mdknuds@sandia.gov.

SUPPLEMENTARY MATERIALS

www.sciencemag.org/content/348/6242/1455/suppl/DC1
Materials and Methods
Figs. S1 to S20
References (*36*–*71*)

22 January 2015; accepted 18 May 2015
10.1126/science.aaa7471

CORAL REEFS

Genomic determinants of coral heat tolerance across latitudes

Groves B. Dixon,[1] Sarah W. Davies,[1] Galina A. Aglyamova,[1] Eli Meyer,[2] Line K. Bay,[3]* Mikhail V. Matz[1]*

As global warming continues, reef-building corals could avoid local population declines through "genetic rescue" involving exchange of heat-tolerant genotypes across latitudes, but only if latitudinal variation in thermal tolerance is heritable. Here, we show an up–to–10-fold increase in odds of survival of coral larvae under heat stress when their parents come from a warmer lower-latitude location. Elevated thermal tolerance was associated with heritable differences in expression of oxidative, extracellular, transport, and mitochondrial functions that indicated a lack of prior stress. Moreover, two genomic regions strongly responded to selection for thermal tolerance in interlatitudinal crosses. These results demonstrate that variation in coral thermal tolerance across latitudes has a strong genetic basis and could serve as raw material for natural selection.

Worldwide, coral reefs are threatened by increasing temperatures associated with climate change (*1*, *2*). Models predict that even a modest increase in the thermal tolerance of reef-building corals over 40 to 80 years would lower their extinction risk dramatically (*3*). Corals are capable of physiological acclimatization to elevated temperature, and it has been argued that in such long-lived organisms acclimatization rather than genetic adaptation will play the leading role in their response to climate change (*4*). Here, we present data for the heritable basis of temperature tolerance that supports the potential for rapid adaptation at the genetic level based on standing genetic variation.

Many coral species maintain high genetic connectivity across thousands of kilometers and inhabit latitudinal ranges that span considerable temperature gradients (*5*, *6*). However, it remains unclear to what extent latitudinal variation in coral thermal physiology is heritable and could fuel genetic rescue via exchange of temperature-tolerant immigrants across latitudes (*7*). We used quantitative genetic, functional genomic, and quantitative trait loci analyses to address this question in *Acropora millepora* corals from thermally divergent locations separated by 5° of latitude: Princess Charlotte Bay (PCB) and Orpheus Island (OI, Fig. 1A).

Ten crosses were established according to a diallel scheme by cross-fertilizing gametes from four adult colonies from the two locations (Fig. 1B). Larval families were cultured in triplicate for 5 days until embryonic development was complete and sampled for tag-based RNA-sequencing analysis (*8*). Separately, larval crosses were scored for heat tolerance, measured as odds of survival after 27 and 31 hours at 35.5°C. The target temperature was reached by ramping over 12 hours at the rate of 0.63°C per hour, less than half of the warming rate on a reef flat during a tidal cycle (*4*).

Survival rates varied substantially among families (Fig. 1D). A mixed-effects generalized linear model with random effects of sire, dam, and their interaction as predictors indicated that the combined parental effects (i.e., broad-sense heritability) accounted for 87% of total deviance in odds of larval survival (Fig. 1E, 95% credible interval of the posterior: 72 to 99%). Proportions of deviance resulting from sire, dam, and their interaction were estimated at 11%, 66%, and 12%, respectively, although the credible intervals were wide because of the limited scope of our crossing design (Fig. 1E). Parents from the warmer location (PCB) conferred significantly higher thermo-tolerance to their offspring relative to parents from the cooler location (OI), with a PCB dam conferring a five-fold increase ($P_{MCMC} < 0.001$; MCMC, Markov chain Monte Carlo) and a PCB sire conferring an additional twofold increase ($P_{MCMC} = 0.048$) in survival odds (Fig. 1F).

To elucidate molecular processes underlying this variation, we identified genes whose expression before stress predicted the odds of larval survival under stress (Fig. 2A), which we term tolerance-associated genes (TAGs). At the 5% false discovery rate (FDR), 1973 TAGs were identified (Fig. 2B). In heat-tolerant larvae, gene ontology (GO) categories related to oxidoreductase activity and extracellular matrix were significantly enriched in the up-regulated gene set, whereas categories related to transmembrane transporter and motor activity were significantly enriched in the down-regulated gene set (Fig. 2C). An analysis of cellular component categories additionally revealed enrichment of nuclear-encoded mitochondrial membrane components (Fig. 2D and fig. S3), potentially a manifestation of mitochondrial variation that could contribute to the high maternal effect on heat tolerance (Fig. 1E).

Higher coral heat tolerance has been attributed to "frontloading," where elevated baseline expression of stress response genes primes the organism for stress (*9*). Alternatively, higher tolerance could be due to the lack of prior stress, in which case the expression of TAGs should be unrelated or opposite to the heat stress response. We compared the TAGs to gene expression in adult parental colonies after 3 days of heat stress (31.5°C, figs. S3 and S4) and to published data on larvae after 4 hours or 5 days of heat stress (*8*), based on patterns of up- and down-regulation within eukaryotic orthologous group (KOG) gene classes (*10*) (Fig. 3A). The adult heat stress response was quite similar to the 5-day larval heat stress response (Fig. 3B). The TAGs expression was significantly negatively correlated with long-term heat stress response in larvae (Fig. 3C) and in adults (albeit marginally significant: $P_{cor.test} = 0.06$). This indicates that the larval heat tolerance we detected most likely arose from the absence of preexisting stress, not from prior up-regulation of heat stress genes through frontloading.

The KOG class most enriched in up-regulated TAGs was energy production and conversion and encompassed mitochondrial proteins (Fig. 3A and fig. S3), further supporting the possible contribution of mitochondrial variation to the maternal effect on heat tolerance (Fig. 1E). Alternatively, maternal effect could be due to epigenetic modification

[1]Department of Integrative Biology, University of Texas at Austin, 205 W. 24th Street C0990, Austin, TX 78712, USA. [2]Department of Integrative Biology, Oregon State University, 3106 Cordley Hall, Corvallis, OR 97331, USA. [3]Australian Institute of Marine Science, PMB 3, Townsville MC, Queensland 4810, Australia.
*Corresponding author. E-mail: l.bay@aims.gov.au (L.K.B.); matz@utexas.edu (M.V.M.)

Direct observation of an abrupt insulator-to-metal transition in dense liquid deuterium

M. D. Knudson *et al.*

Science **348**, 1455 (2015);
DOI: 10.1126/science.aaa7471